Appl. Phys. B (2013) 113:87–92
DOI 10.1007/s00340-013-5664-2

Applied Physics B
Lasers and Optics

RAPID COMMUNICATION

Volume-resolved flame chemiluminescence and laser-induced fluorescence imaging

Mark L. Greene · Volker Sick

Received: 31 May 2013 / Accepted: 20 September 2013 / Published online: 2 October 2013

Abstract There is significant need for optical diagnostic techniques to measure instantaneous volumetric vector and scalar distributions in fluid flows and combustion processes. This is especially true for investigations where only limited optical access is available, such as in internal combustion engines, furnaces, flow reactors, etc. While techniques such as tomographic PIV for velocity measurement have emerged and reached a good level of maturity, instantaneous 3D measurements of scalar quantities are not available at the same level. Recently, developments in light field technology have progressed to a degree where implementation into scientific 3D imaging becomes feasible. Others have already demonstrated the utility of light field technology toward imaging high-contrast particles for PIV and for imaging flames when treated as single-surface objects. Here, the applicability and shortcomings of current commercially available light field technology toward volumetric imaging of translucent scalar distributions and flames are investigated. Results are presented from imaging canonical chemiluminescent and laser-induced fluorescent systems. While the current light field technology is able to qualitatively determine the position of surfaces by locating high-contrast features, the correlation-based reconstruction algorithm is unable to fully reconstruct the imaged objects for quantitative diagnostics. Current analysis algorithms are based on high-contrast correlation schemes, and new tools, possibly based on tomographic concepts, will have to be implemented to reconstruct the full 3D structure of translucent objects for quantitative analysis.

M. L. Greene (✉) · V. Sick
Department of Mechanical Engineering, University of Michigan, 1231 Beal Avenue, Ann Arbor, MI 48109-2133, USA
e-mail: mlgreene@umich.edu

1 Introduction

Few flow and combustion processes are steady in nature or less than 3D in space, and comprehensive studies ultimately require full 3D resolution along with observation rates that adequately resolve the temporal evolution [1]. In particular, for combustion processes, the nonlinear coupling of physical and chemical processes makes it difficult to reduce the dimensionality of the problem without losing important aspects. 3D measurements with adequate data acquisition rates must capture velocity, temperature, chemical species, and phase distributions, to provide relevant qualitative and quantitative information. Efforts to develop 3D imaging capabilities have been made for some time in a variety of fields [2]. In combustion research, these include techniques of simultaneously utilizing multiple light sheets [3], a moving light sheet [4], holographic approaches [5], and tomographic methods [6]. For scalar imaging, these techniques offer only quasi-3D measurements at best, as the entire volume cannot be imaged simultaneously. For velocity measurements, tomographic PIV offers a sophisticated approach requiring 4–6 cameras with independent fields of view [7]. While tomographic PIV offers excellent 3D reconstruction of the flow field, it is a tedious system to calibrate and requires nearly unobstructed optical access. Unfortunately many interesting problems in fluid mechanics provide limited optical access, which prevents the application of tomographic PIV as a solution for 3D velocimetry in these studies. The need for a technique to capture truly instantaneous 3D scalar fields and/or 3D velocity measurements in applications with limited optical access is tremendous, but of course difficult to achieve. An example of a high frame rate single-camera 3D velocimetry technique for measurements in locations with limited optical access was developed for short

working distances and smaller volumes [8]. Another example of a single-camera 3D velocimetry technique, but with low frame rates, was demonstrated with a plenoptic camera [9]. But the challenge remains to achieve instantaneous 3D-resolution for scalar quantities such as species concentrations or temperature, and to obtain these measurements for larger volumes while still achieving adequate spatial resolution.

An opportunity exists to develop such imaging capability based on light field technology with a plenoptic camera. A 'light field' is the representation of an object when both the origin and direction of each ray is recorded. A plenoptic camera captures the light field of an object by utilizing a traditional camera lens as a main objective to produce a real image, which is then reimaged by a micro-lens array to produce many micro-images on the sensor. The short focal distance of the micro-lenses compared to the array dimensions allow each lens to produce an image of the object from a unique perspective and field of view. This concept was introduced by G. Lippmann in 1908 [10]. Regardless of sensor type, all raw plenoptic camera images require extensive post-processing to derive 3D images. The quality of the resulting 3D reconstruction can substantially depend on parameter selection for the post-processing procedure. Using the techniques sketched by Perwaß and Wietzke [11], the depth of focus and spatial resolution of a plenoptic camera can be optimized by using a micro-lens array populated with lenses of differing focal lengths. They have also shown that a plenoptic camera equipped with micro-lenses of three focal lengths in a regular hexagonal grid can achieve a spatial resolution in the third dimension of one quarter the resolution of the raw image sensor.

Applications for light field cameras have begun to emerge and find their way into combustion research. The use of light field photography for 3D velocity field measurements has been demonstrated [9]. Mie scattering from particles dispersed in water analogue internal combustion engine flow was reconstructed to yield the 3D velocity field [9]. More recently, the applicability of light field photography using flame single-surface reconstruction was demonstrated in an opposed multi-burner gasifier [12].

As the depth estimation process is currently based on a cross-correlation algorithm of local contrast between neighboring micro-images, arriving at physically valid depth estimations requires the image to contain localized high-contrast features. This is a significant limitation in imaging chemiluminescence and scalar 3D distributions with low spatial gradients in the scalar quantity. Here, we test the limits of operation and applicability of correlation-based light field technology to volumetrically resolve the low-contrast systems often characteristic of experiments utilizing chemiluminescence and laser-induced fluorescence. Both of these experiments are important tools commonly used in combustion research, and the chosen conditions have fundamentally different intensity distributions. The premixed flame imaged in these experiments has an intensity distribution originating from the thin reactive shell on its periphery, whereas that of the laser-induced fluorescence system is proportional to the continuous volumetric distribution of a fluorescent tracer.

2 Experiment

Images were acquired with a 29-megapixel color plenoptic camera (Raytrix R29) and were processed with the associated software package (RxLive 2.8.61.0). This camera uses a micro-lens array with lenses of three different focal lengths, which enables two features. First, increased depth resolution and second, increased lateral resolution in the final image [11], i.e., up to 3,288 × 2,192 pixels in this particular case.

The underlying approach of the 3D reconstruction is based on a cross-correlation algorithm that determines the location of regions in neighboring micro-images where the same part of the object is represented. For the cross-correlation to work, high-contrast features, i.e., strong spatial intensity gradients, are required. The optical parameters of the objective lens and micro-lenses are then used to estimate the depth and intensity of high-contrast features in the matching regions [11]. The size of the interrogation windows used for the correlation algorithm and the pixel displacement between neighboring windows are adjustable. This step is similar in nature to typical particle image velocimetry analysis approaches. The minimum local contrast in interrogation windows to be used for correlation and the minimum correlation value required to calculate a depth estimate are user adjusted during post-processing, and are individually tuned for each focal length lens type in the micro-lens array. It is essential that the images contain sufficient contrast, and therefore, the post-processing steps may include user-controlled contrast enhancements, as well as thresholding, to remove or reduce signals below a freely selectable level. While this improves the quality of the cross-correlation, it removes the initial linear relationship between incoming light intensity and recorded intensity values in the output images. Calibration of signals to physical light intensity, or a corresponding concentration of a molecular species, is therefore lost in this case.

The reconstruction settings require two calibration steps. First, an algorithm is run to adapt the software to the optical settings and second, the scaling of the third dimension is calibrated to external references. The first step is needed to determine the location of the micro-images on the sensor. A diffuser plate (ExpoDisc, 67 mm) mounted to the front lens creates a sufficiently uniform

illumination to produce a pattern of spots on the sensor that reflect the position of the lenslets in the micro-lens array. The external calibration was necessary to determine the proportionality constant between the reconstructed depth response of the camera and physical object distance. This was achieved by recording three reconstructed depths for each millimeter of a 0–13 mm translation of a target mounted to a translation stage. The process was repeated for each set of depth calculation parameters used for the experiments described here. The reconstructed depth versus distance curve is linear in distance with a sensitivity of 0.50 ± 0.01 mm^{-1}.

The capability of cross-correlation-based light field photography to fully resolve 3D chemiluminescence and scalar imaging was tested in two separate experiments. A commercial propane-fueled soldering torch was chosen as an example of a high-contrast flame chemiluminescence experiment. In this burner, the luminosity comes purely from a thin reactive shell at the outer surface of the premixed flames. A faint enveloping outer diffusion flame is not visible in the photographs presented. The second experiment tested a 3D volume intensity distribution created by laser-induced fluorescence of a pair of acetone-seeded nitrogen jets. This second experiment was chosen to test the camera technology in a fundamentally different way than with the torch, as here the luminosity is produced uniformly throughout the illuminated volume with sharper edges only at the jet boundaries. The treatment and extraction of the volume-resolved data from these translucent systems is discussed in the results section of this paper.

The torch was orientated such that the gases exited the nozzle nearly horizontal. Signals were collected and imaged onto the camera chip without any spectral filtering using a 200 mm main objective at a working distance of 500 mm and an f-stop setting of 8 to match that of the micro-lenses, in order for the micro-images to fill the image sensor without overlapping. The camera was triggered internally with an exposure time of approximately 100 ms when imaging the propane torch. The geometries of both experiments allow measurements free of reflections and glare background, and thus, any non-signal contribution in the images can be considered noise. While the minimum exposure time of the camera is about 100 µs, the long exposure time was necessary to accumulate enough signal on the chip to achieve an acceptable signal-to-noise ratio of 23, where the *S/N* is calculated by

$$S/N = \frac{\mu_{\text{signal}} - \mu_{\text{background}}}{\text{rms}_{\text{background}}} \quad (1)$$

by evaluating two 20 × 20 pixel regions taken on the flame (signal) and on a dark region of the image (background) and where μ_i is the mean pixel count in the regions.

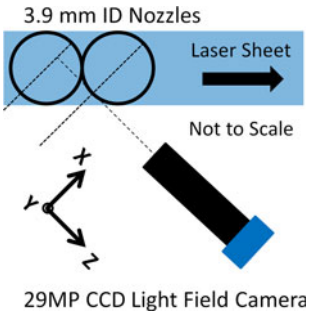

Fig. 1 Illustration of laser beam arrangement used to excite the two acetone-doped jets mixing in air as viewed into the nozzles

Figure 1 presents the optical setup used for the LIF experiment. Nitrogen was metered through a mass flow controller and seeded with acetone at room temperature to serve as a fluorescent tracer by passing through a gas-washing bottle. The nitrogen flow rate was 5 slpm, and jets were formed by a pair of vertically oriented tubes (3.9 mm inside diameter) aligned perpendicular to the light sheet and spatially separated by 6.35 mm on center. An exhaust vent was placed 70 mm above the nozzles, which were flowing in the positive y direction as shown by the axes in Fig. 1; 266 nm radiation from a frequency-quadrupled Nd:YAG laser (Continuum Surelite III) was passed through dielectric beam splitters and a Pellin-Broca prism to remove residual long wavelengths before exciting the acetone. The beam was focused vertically with a +500-mm-cylindrical lens placed 480 mm from the jets to increase the sheet intensity while still illuminating the full width of the jets at a height of 1 mm above the nozzle exits. The camera was triggered from a 5-Hz signal derived from the laser Q-switch output by a digital delay generator. The main objective lens settings were the same as for the flame chemiluminescence. The laser was operated at 10 Hz with average pulse energies of 48 mJ. Despite this high pulse energy, the camera exposure time had to be set to 500 ms to accumulate signals from five consecutive laser pulses, obtaining an *S/N* of 56 in the raw image.

3 Results and discussion

The results of the chemiluminescence measurement are presented in Fig. 2. Figure 2a depicts the refocused image of the torch flame, which is a 2D projection of the 3D image as viewed from large values of *z* and is equivalent to what would have been acquired with a traditional camera. The image was acquired from a line of sight perpendicular to the *x*–*y* plane in order to increase the difficulty of the proceeding depth estimation as all three flames originate from the same plane parallel to the optical axis. In this case, the middle flame is indeed the closest to the camera of

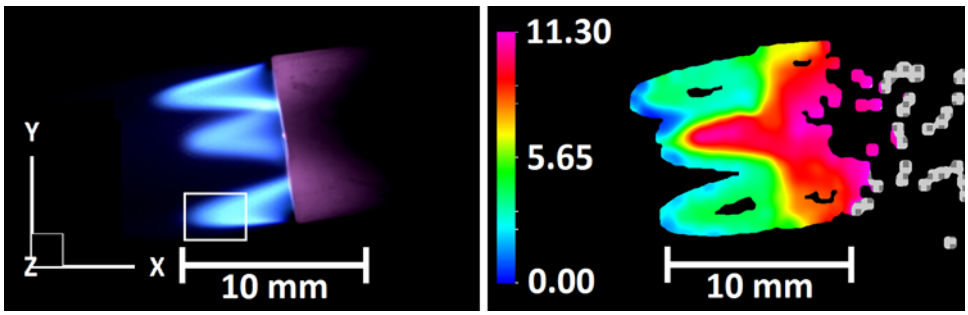

Fig. 2 **a** Refocused image of torch (*left*), and **b** color depth map of torch (*right*). The *white square* shown in the *left image* denotes the region that is highlighted in Fig. 3

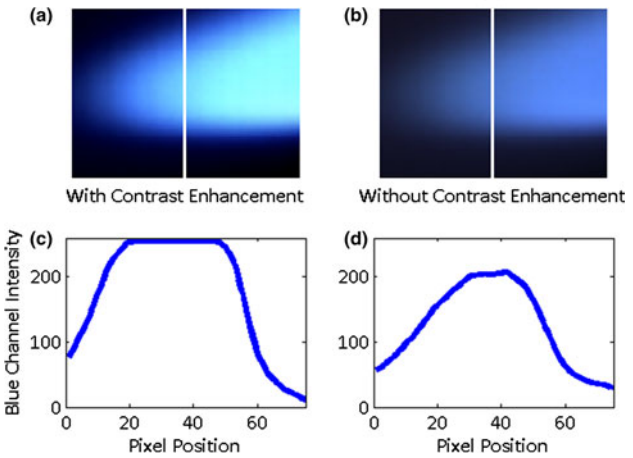

Fig. 3 **a** Close-up of marked region in Fig. 2a, b same region when contrast enhancement is turned off, **c** *blue channel line* intensity profile for (**a**), and **d** *blue channel line* intensity profile for (**b**). The linear relationship between signal intensity and acetone concentration has been destroyed in (**a**) and (**c**), but is present in the unaltered images in (**b**) and (**d**)

the three flames exiting the nozzle despite the illusion otherwise. Figure 2b shows the calculated depth of the image structure where blues are located farther from the camera and reds are closer to the camera. The gaps in the depth values shown in Fig. 2b are low-contrast areas that were excluded by the algorithm. The white and gray checkered spots on the right in Fig. 2b are outside the calibrated range for the third dimension and have to be considered artifacts of the reconstruction.

The contrast-based correlation algorithm used for the depth estimation requires high-contrast structures upon which to calculate the depth. It was necessary to drastically enhance the contrast of the image by increasing the brightness and contrast settings of the raw image before calculating the depth map. Image brightness was increased by multiplying the intensity values so that peak values reached the upper end of the dynamic range. Increasing the contrast stretched the recorded intensities to the lower and higher end of the dynamic range around the middle intensity value, in this case 127 counts. Values that reach or exceeded the lower or upper limit are set to that respective value. Finally, a lower threshold was set below which all values were set to zero (contrast offset) to reduce background levels and to artificially increase the resulting signal-to-noise ratio. The combined effect of these processes on the images is demonstrated in Fig. 3. The steeper intensity gradient shown in Fig. 3a aids the depth estimation process and yields a more reliable result than the more diffuse edge shown in Fig. 3b, when the contrast enhancement has been turned off. Figure 3c, d shows the blue channel line intensity profiles over the pixel columns marked white in Fig. 3a, b, respectively. In post-processing, median and mean filters were applied to smooth the depth map after it was calculated. A close examination of Fig. 2b indicates an apparent swelling of the flames compared to the photograph shown in Fig. 2a. This is due to an additional and final post-processing step used to fill in the depth field by interpolating from the sparsely populated depth map that was originally calculated.

The camera's software is optimized for surface imaging applications and prevents more than one depth value to be displayed for each pixel in the lateral plane. This means that the camera's software prevents the rear surfaces of the flames from being displayed. However, in the analysis of the raw images, such information is generated and available for export to external software prior to any post-processing steps. As these data are exported before the final post-processing steps of filtering and interpolating the depth field, it was necessary to apply either a filter or outlier removal algorithm to the exported data. An outlying point detection process was applied where points with a nearest neighbor distance greater than the mean were removed. These points were plotted using the RGB intensities calculated by the camera, but given that the CH* chemiluminescence (430 nm) dominates the emission from the flame cones, only the blue channel has measureable signal.

Figure 4 presents the resulting scatterplot viewed toward the positive x-axis or in the upstream direction of the burner. Note that the points from the nozzle surface have been removed and replaced by a circle for clarity. The three flames are clearly distinguishable as general regions of highest population, although there are several significant

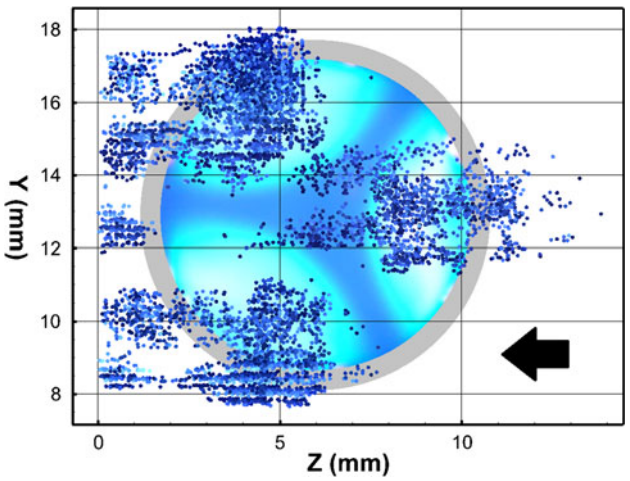

Fig. 4 Scatterplot looking into the nozzle of the torch. The *arrow* indicates the line of sight of the camera, and the *point colors* are the RGB values recorded by the camera. A traditional 2D image of flame geometry is displayed in the background

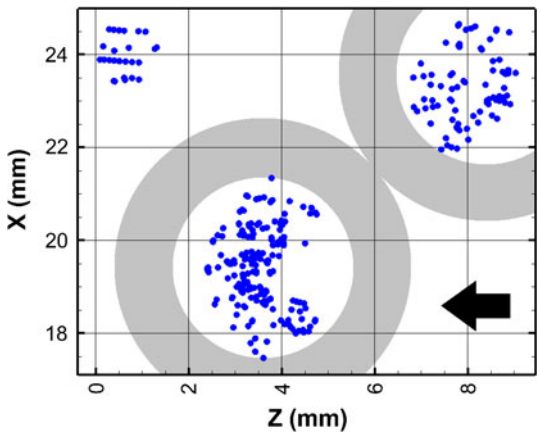

Fig. 6 Acetone-seeded jets viewed from above. The *arrow* indicates the camera line of sight, and the *colors* are the RGB values recorded by the camera

nonphysical artifacts in the image that lie outside of the nozzle represented in gray.

Figure 5 presents the results of the scalar acetone experiment in the same format as shown previously in Fig. 2. Figure 6 presents an analogous scatterplot image to Fig. 4 of the acetone jets viewed from above. The improved depth estimation from the contrast enhancement does come at the expense of quantitative measurements from the intensity values, as the linearity between concentration and intensity has been destroyed. Links between the signal and the concentration of acetone cannot be made at this time.

4 Conclusions

The existing camera technology was able to adequately estimate the depth of the front surfaces of three premixed flames exiting the nozzle of a soldering torch, as well as the front surfaces of a pair of acetone-seeded nitrogen jets mixing in air. However, the reconstruction algorithm was unable to reconstruct the back surface of these diffuse objects without producing nonphysical artifacts to the rear side of the structures.

There are three main limitations of the current technology toward suitability for imaging translucent systems. Firstly, the correlation-based reconstruction algorithm functions poorly in the low-contrast features characteristic of chemiluminescent and fluorescent systems. Secondly, the small pixel size of 5.5 μm, the concentration of CL/LIF signals in the blue channel, the required small aperture, and the presence of the micro-lens array all combine to greatly reduce signal intensity through the system. This decreases the signal-to-noise ratio where the noise in the background of the image interferes with the depth calculation. The background can be removed electronically, but at the cost of destroying the linearity between LIF signal and the measured scalar quantity. This couples with the poor performance of the reconstruction algorithms to make calculation of the depth quite challenging. Lastly, a priori knowledge of the system is required to reconstruct the scene using the multitude of adjustable parameters used by the reconstruction algorithm.

While the results for these specific experiments could be marginally improved through the use of a monochrome camera with a lower f/# micro-lens array, it would not improve the fundamental weakness of the contrast-based reconstruction process. For these reasons, we believe the future of light field technology for volumetric imaging of translucent systems would benefit from a tomographic reconstruction approach rather than the algorithms

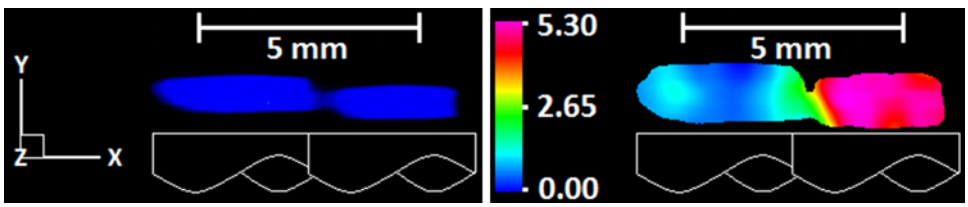

Fig. 5 **a** Refocused image of acetone-seeded jets (*left*), and **b** color depth map of acetone-seeded jet (*right*)

currently applied [13, 14]. Development in this area is necessary for the acquisition of high-fidelity volume-resolved data from chemiluminescence and laser-induced fluorescence measurements.

Acknowledgments This material is based upon work supported by the National Science Foundation under Grant No. 1032930. The authors would like to acknowledge K. Peterson at General Motors R&D for his encouragement and interest in pursuing this work, and L. Wietzke and C. Perwaß of Raytrix GmbH for fruitful discussions and input.

References

1. V. Sick, Proc. Combust. Inst. **34**(2), 3509–3530 (2013)
2. X. Xiao, B. Javidi, M. Martinez-Corral, A. Stern, Appl. Opt. **52**(4), 546–560 (2013)
3. J. Nygren, J. Hult, M. Richter, M. Alden, M. Christensen, A. Hultqvist, B. Johansson, 29th Symp. (Int) Combust. (2002), pp. 679–685
4. R. Wellander, M. Richter, M. Alden, Opt. Express **19**(22), 21508–21514 (2011)
5. J.M. Coupland, C.P. Garner, R.D. Alcock, N.A. Halliwell, J. Phys. Conf. Ser. **45**, 29–37 (2006)
6. V. Sick, H. McCann, in *Process Imaging for Automatic Control*, eds. by H. McCann, D. Scott (CRC Press, Taylor & Francis Group, Boca Raton, 2005), pp. 263–297
7. G.E. Elsinga, F. Scarano, B. Wieneke, B.W. Oudheusden, Exp. Fluids **41**(6), 933–947 (2006)
8. K. Peterson, B. Regaard, S. Heinemann, V. Sick, Opt. Express **20**(8), 9031–9037 (2012)
9. T. Nonn, J. Kitzhofer, D. Hess, C. Brücker, in *16th International Symposium on Applications of Laser Techniques to Fluid Mechanics*, Lisbon, Portugal, 2012
10. G. Lippmann, Comptes Rendus de l'Académie des Sciences **146**(9), 446–551 (1908)
11. C. Perwaß, L. Wietzke, Human Vision and Electronic Imaging XVII, Burlingame, California, USA, 22 Jan 2012, p. 829108
12. Y. Gong, Q. Guo, J. Zhang, P. Fan, Q. Liang, G. Yu, Ind. Eng. Chem. Res. **52**, 3007–3018 (2013)
13. Y. Zhang, H.-P. Chan, B. Sahiner, J. Wei, M.M. Goodsitt, L.M. Hadjiiski, J. Ge, C. Zhou, Med. Phys. **33**(10), 3781–3795 (2006)
14. J.T. Dobbins III, D.J. Godfrey, Phys. Med. Biol. **48**, R65–R106 (2003)